# XANES and EXAFS Studies on the Ir−O Bond Covalency in Ionic Iridium Perovskites

**Jin-Ho Choy,*,† Dong-Kuk Kim,† Sung-Ho Hwang,† Gérard Demazeau,‡ and Duk-Young Jung‡**

*Contribution from the Department of Chemistry, Center for Molecular Catalysis (CMC), College of Natural Sciences, Seoul National University, Seoul 151-742, Korea, and Institut de Chimie de la Matière de Condenseé de Bordeaux (ICMCB), 33600 Pessac Cedex, France*

*Received February 13, 1995*®

**Abstract:** X-ray absorption spectroscopic studies have been systematically carried out at the Ir $L_{III}$-edge for a series of perovskite compounds, $A_2BIrO_6$ (A = Ba, Sr, and La; B = Zn, Mg, Y, Ca, Li, and Sr), in which the iridium ions with various oxidation states +IV ($d^5$), + V ($d^4$), and +VI ($d^3$) are stabilized in an octahedral site of oxide lattices in order to obtain electronic and local structural information on the iridium upon the change of its oxidation state. On the basis of one-electron approximation and crystal field theory, XANES spectra for the present compounds clearly showed that the white line shapes and positions reflect the local site symmetry and oxidation state of the absorbing iridium atom well. The transition to $e_g$ states oriented directly to oxygen ligands in $O_h$ symmetry is influenced more than that to $t_{2g}$ states by the change of oxidation state. A precise inspection of the white line positions indicated to us that the transition metal ion with a high oxidation state would be more preferable to induce a variety of physicochemical properties through the change in chemical environments. A good linear relationship is observed between the difference in peak areas for each transition state and the oxidation state of the iridium. It has been quantitatively studied how the A cation size and the ionicity of the B−O bond could influence the covalency of the Ir−O bond. By means of EXAFS analysis, the ionic radius of octahedrally coordinated $Ir^{VI}$ could be determined to be 0.521 Å from the average Ir−O bond distances for each oxidation state of the iridium and Shannon's ionic radii of $Ir^{III}$, $Ir^{IV}$, and $Ir^{V}$ ions. A linear relationship between the Debye−Waller factors and the Ir−O bond distances suggests that the $IrO_6$ octahedron in the present compounds is nearly regular irrespective of the crystal symmetries. Effects of the oxidation state of the probed metal ions on the EXAFS analysis also have been examined.

## Introduction

Recently, X-ray absorption spectroscopy has been revealed to be a potential tool for determining electronic and geometrical structures. In particular, $L_{II,III}$-edge X-ray absorption spectra of transition metals have been the topic of several studies since they could probe orbitals with d character that are the primary orbitals involved in the chemical bonding between the transition metal and the ligand.[1−26] However, there are only a few publications on $L_{II,III}$-edge X-ray absorption spectroscopy of the third-row transition metals in complex metal oxides.[1−3] Furthermore, since there are several factors such as the effect of chemical environment on absorbing atoms and bonding character between the metal and the ligand that are relevant to the interpretation of X-ray absorption spectra, a systematic survey of the experimental aspects of $L_{III}$-edge X-ray spectroscopy is necessary.

In this regard, perovskite compounds with the general formula $A_2BB'O_6$ are good candidates because all constituent atoms are positioned in the structurally well-characterized sites and

† Seoul National University.

‡ Institut de Chimie de la Matière de Condenseé de Bordeaux (ICMCB).

® Abstract published in *Advance ACS Abstracts,* July 15, 1995.

(1) Choy, J. H.; Kim, D. K.; Demazeau, G.; Jung, D. Y. *J. Phys. Chem.* **1994**, *98*, 6258.

(2) Bare, S. R.; Mitchell, G. E.; Maj, J. J.; Vrieland, G. E.; Gland, J. L. *J. Phys. Chem.* **1993**, *97*, 6048.

(3) Pendharkar, A. V.; Mande, C. *Chem. Phys.* **1975**, *7*, 244.

(4) Bianconi, A.; Budnick, J.; Chamberland, B.; Clozza, A.; Dartyge, E.; Demazeau, G.; De Santis, M.; Flank, A. M.; Fontain, A.; Jegoudez, J.; Lagarde, P.; Lynds, L. L.; Michel, C.; Otter, F. A.; Tolentino, H.; Raveau. B.; Revcolevschi, A. *Physica C* **1988**, *153−155*, 113.

(5) Brown, M.; Peierls, R. E.; Stern, E. A. *Phys. Rev. B* **1977**, *15*, 738.

(6) Lytle, F. W. *J. Catal.* **1976**, *43*, 376.

(7) Wei, P. S. P.; Lytle, F. W. *Phys. Rev. B* **1979**, *19*, 679.

(8) Lytle, F. W.; Wei, P. S. P.; Greegor, R. B.; Via, G. H.; Sinfelt, J. H. *J. Chem. Phys.* **1979**, *70*, 4849.

(9) Horsley, J. A. *J. Chem. Phys.* **1982**, *76*, 1451.

(10) Sham, T. K. *J. Am. Chem. Soc.* **1983**, *105*, 2269; *J. Chem. Phys.* **1985**, *83*, 3222; *Phys. Rev. B* **1985**, *31*, 1888, 1903.

(11) Mansour, A. N.; Cook, J. W., Jr.; Sayers, D. E. *J. Phys. Chem.* **1984**, *88*, 2330.

(12) Koch, E. E.; Jugnet, Y.; Himpsel, F. J. *Chem. Phys. Lett.* **1985**, *116*, 7.

(13) Thole, B. T.; Cowan, R. D.; Sawatzky, G. A.; Fink, J.; Fuggle, J. C. *Phys. Rev. B* **1985**, *31*, 6856.

(14) Sugiura, C.; Kitamura, M.; Muramatsu, S. *J. Chem. Phys.* **1986**, *84*, 4824; *Phys. Status Solidi B* **1987**, *140*, 631; *J. Phys. Chem. Solids* **1988**, *49*, 1095.

(15) Qi, B.; Perez, I.; Ansari, P. H.; Lu, F.; Croft, M. *Phys. Rev. B* **1987**, *36*, 2972.

(16) Hedman, B.; Frank, P.; Gheller, S. F.; Roe, A. L.; Newton, W. E.; Hodgson, K. O. *J. Am. Chem. Soc.* **1988**, *110*, 3798.

(17) van der Laan, G.; Thole, B. T.; Sawatzky, G. A.; Verdaguer, M. *Phys. Rev. B* **1988**, *37*, 6587.

(18) Thole, B. T.; van der Laan, G.; Butler, P. H. *Chem. Phys. Lett.* **1988**, *149*, 295.

(19) de Groot, F. M. F.; Fuggle, J. C.; Thole, B. T.; Sawatzky, G. A. *Phys. Rev. B* **1990**, *41*, 928; **1990**, *42*, 5459.

(20) Lytle, F. W.; van der Laan, G.; Greegor, R. B.; Larson, E. M.; Violet, C. E.; Wong, J. *Phys. Rev. B* **1990**, *41*, 8955.

(21) George, G. N.; Cleland, W. E., Jr.; Enemark, J. H.; Smith, B. E.; Kipke, C. A.; Roberts, S. A.; Cramer, S. P. *J. Am. Chem. Soc.* **1990**, *112*, 2541.

(22) George, S. J.; van Elp, J.; Chen, J.; Ma, Y.; Chen, C. T.; Park, J. B.; Adams, M. W. W.; Searle, B. G.; de Groot, F. M. F.; Fuggle, J. C.; Cramer, S. P. *J. Am. Chem. Soc.* **1992**, *114*, 4426.

(23) van der Laan, G.; Kirkmann, I. W. *J. Phys.: Condens. Matter* **1992**, *4*, 4189.

(24) Brydson, R.; Garvie, L. A. J.; Craven, A. J.; Sauer, H.; Hoger, F.; Cressey, G. *J. Phys.: Condens. Matter* **1993**, *5*, 9379.

(25) Moraweck, B.; Renouprez, A. J.; Hill, E. K.; Baudoning-Savois, R. *J. Chem. Phys.* **1993**, *97*, 4288.

(26) Pearson, D. H.; Ahn, C. C.; Fultz, B. *Phys. Rev. B* **1993**, *47*, 8471.

0002-7863/95/1517-8557$09.00/0 

transition metal ions (B′) with various oxidation states can be stabilized by adequately controlling structural and chemical factors such as the type of A or B element and synthetic conditions (i.e. high oxygen pressure). For these reasons, we have previously reported[1] some results on iridium $L_{III}$-edge XANES (X-ray absorption near-edge structure) spectra for the perovskite compounds $La_2MgIrO_6$, $La_2LiIrO_6$, and $Ba_2CaIrO_6$ having the oxidation states of $Ir^{IV}$, $Ir^{V}$, and $Ir^{VI}$, respectively, in which it has been shown that $L_{III}$-edge XANES spectroscopy is a useful tool for characterizing d states of the transition metal and the metal−ligand bonding nature on the basis of one-electron approximation and crystal field theory. Mainly it was found that the white line areas of $L_{III}$-edge XANES spectra are very sensitive to the occupation of d states, and thus such a correlation between hole densities in solids and the white line areas could be extensively applied to investigate the hole densities and local site symmetries of other transition metals. In this study, however, an attempt was made to combine XANES and EXAFS (extended X-ray absorption fine structure) complementarily for providing not only electronic structural information of the iridium ions but also local structural information on the neighboring atoms of the iridium ions. In addition, the analyses of X-ray absorption spectra for a larger number of iridium compounds would give more definitive and general information concerning the substantial aspects of the change of chemical environments and oxidation states of the iridium by reducing the statistical uncertainties.

We have therefore examined extensively how the oxidation state of the iridium and the nature of A and B atoms could be influenced by the crystal field of the iridium site in the perovskite lattice of $A_2BIrO_6$ (A = Ba, Sr, and La; B = Sr, Ca, Zn, Mg, Li), which quantitatively illustrates the degree of covalency in the Ir−O bond. To our knowledge, it is very difficult to obtain directly the crystal field strength from the optical spectroscopic method for the perovskite compounds because d−d transitions are overlaid by the intense ligand-to-metal charge transfer (LMCT) transition in most cases. Furthermore, all the present Ir perovskites are black and thus not transparent in the ultraviolet and visible regions. For these reasons, the covalency of the B′−O bond in the $A_2BB'O_6$ perovskite compounds has been estimated qualitatively by examining the ionicities of the A−O and B−O bonds which compete with the B′−O bond by sharing the same oxygen 2p orbitals with the pathway of 90° and 180°, respectively.[27−34] We believe therefore that the present work on the relative crystal field strength of the iridium site has provided the first quantitative results about the bonding character of the transition metal−ligand bond in the perovskite lattice.

Various oxidation states of $Ir^{IV}$, $Ir^{V}$, and $Ir^{VI}$ in the perovskite oxide compounds are of great interest because the Ir−O bond lengths depend on the local structure and the chemical environments. Even though the crystal structures of the present perovskites can be well-determined by the conventional X-ray diffraction method, EXAFS analysis also has some significant meaning complementary to the X-ray diffraction results. First, single crystals for the complex perovskite oxides are difficult to obtain and the powder X-ray diffraction method might induce an uncertainty for determining the appropriate space group and oxygen coordinates in the compounds with a small distortion from the ideal perovskite structure.[35−37] Second, there are often cases where A/A′ or B/B′ cations are partially disordered in the perovskite compound having the general formula $AA'BB'O_6$. Therefore the EXAFS spectroscopy, which is very sensitive to short-range coordination about a specific element, could give more precise information on the local structure around the iridium ions.

## Experimental Section

**Sample Preparation.** Polycrystalline samples of $Ba_2MIrO_6$ (M = Sr, Ca, Y, and Zn),[38−40] $Sr_2M'IrO_6$ (M′ = Ca, and Mg), $La_2M''IrO_6$ (M″ = Mg, and Zn),[41−43] $BaLaLiIrO_6$,[40] and $La_2LiIrO_6$[44,45] were prepared by calcining stoichiometric amounts of reactants $BaCO_3$, $SrCO_3$, $CaCO_3$, $La(CH_3CO_2)_3$, ZnO, $Y_2O_3$, $[4(MgCO_3)\cdot Mg(OH)_2\cdot 5H_2O]$, $IrO_2$, and excess $Li(OH)\cdot H_2O$ in order to compensate a loss during the high-temperature synthesis. The reaction mixture was heated at the following temperature for several days in an oxygen flow of 1 bar, with frequent regrinding: $La_2LiIrO_6$ and $BaLaLiIrO_6$ at 800 °C and the other samples at 950 °C. $Sr_2CaIrO_6$ and $Ba_2YIrO_6$ were treated again at 1100 °C in air for 24 h in order to obtain a good crystallinity. And then the oxygen gas pressure of 2 kbar and 600 bar using a compressed-gas apparatus was applied for the lithium-containing compounds at 800 °C and for $Ba_2MIrO_6$ (M = Sr, Ca, Y, and Zn) and $Sr_2M'IrO_6$ (M′ = Ca and Mg) at 880 °C for 48 h, respectively, to stabilize the high oxidation states of the iridium (+V, and +VI). In order to reduce oxygen deficiency, $Ir^{VI}$ perovskite compounds were finally re-treated at the same temperatures for 10−15 min under high oxygen pressure of 60−75 kbar; such a high pressure could only be generated in situ by thermal decomposition of $KClO_3$, which was already intermixed with samples before they were set in a belt-type high-pressure apparatus. $SrIrO_3$[46,47] was obtained by the solid state reaction of $SrCO_3$ and $IrO_2$ at 900 °C under a 1-bar oxygen atmosphere for 48 h. For preparing the orthorhombic $SrIrO_3$ perovskite, the sample was heated at 1100 °C for 30 min without $KClO_3$ under 70 kbar of pressure in a belt-type apparatus.

**Chemical Titration.** The oxidation state of the iridium was determined by iodometric titration using sodium thiosulfate solution with a starch indicator. The reaction scheme for the reduction of iridium by iodide is the following:

$$(x-3)I^{-1} + Ir^{+x} \rightarrow [(x-3)/2]I_2 + Ir^{+III}$$

The back-titration method using Mohrs salt was also adopted for $Sr_2$-

(27) Demazeau, G.; Buffat, B.; Menil, F.; Fournes, F.; Pouchard, M.; Dance, J. M.; Fabritchnyi, P.; Hagenmuller, P. *Mater. Res. Bull.* **1981**, *16*, 1465.
(28) Demazeau, G.; Pouchard, M.; Chevreau, N.; Thomas, M.; Menil, F.; Hagenmuller, P. *Mater. Res. Bull.* **1981**, *16*, 689.
(29) Demazeau, G.; Marty, J. L.; Pouchard, M.; Rojo, T.; Dance, J. M.; Hagenmuller, P. *Mater. Res. Bull.* **1981**, *16*, 47.
(30) Demazeau, G.; Marty, J. L.; Buffat, B.; Dance, J. M.; Pouchard, M.; Dordor, P.; Chevalier, B. *Mater. Res. Bull.* **1982**, *17*, 37.
(31) Choy, J. H.; Demazeau, G.; Byeon, S. H.; Dance, J. M. *J. Phys. Chem. Solids* **1990**, *51*, 391.
(32) Choy, J. H.; Demazeau, G.; Dance, J. M. *J. Solid State Chem.* **1990**, *84*, 1.
(33) Byeon, S. H.; Demazeau, G.; Dance, J. M.; Choy, J. H. *Eur. J. Solid State Inorg. Chem.* **1991**, *28*, 643.
(34) Byeon, S. H.; Demazeau, G.; Fournes, L.; Dance, J. M.; Choy, J. H. *Solid State Commun.* **1991**, *80*, 457.
(35) Choy, J. H.; Demazeau, G.; Hong, S. T. *Jpn. J. Appl. Phys.* **1992**, *31*, 3649.
(36) Demazeau, G.; Oh-Kim, E. O.; Choy, J. H.; Hagenmuller, P. *J. Solid State Chem.* **1992**, *101*, 221.
(37) Choy, J. H.; Demazeau, G.; Dance, J. M.; Byeon, S. H.; Müller, K. A. *J. Solid State Chem.* **1994**, *109*, 289.
(38) Demazeau, G.; Jung, D. Y.; Sanchez, J. P.; Colineau, E.; Blaise, A.; Fournes, L. *Solid State Commun.* **1993**, *85*, 479.
(39) Jung, D. Y.; Gravereau, P.; Demazeau, G. *Eur. J. Solid State Inorg. Chem.* **1993**, *30*, 1025.
(40) Demazeau, G.; Jung, D. Y. Studies of several compounds will be published elsewhere, and the results are obtained by private communication.
(41) Blasse, G. *J. Inorg. Nucl. Chem.* **1965**, *27*, 993.
(42) Powell, A. V.; Gore, J. G.; Battle, P. D. *J. Alloys Compds.* **1993**, *201*, 73.
(43) Ralos, E. M.; Alvarez, I.; Veiga, M. L.; Pico, C. *Mater. Res. Bull.* **1994**, *29*, 8.
(44) Hayashi, K.; Demazeau, G.; Pouchard, M.; Hagenmuller, P. *Mater. Res. Bull.* **1980**, *15*, 461.
(45) Darriet, J.; Demazeau, G.; Pouchard, M. *Mater. Res. Bull.* **1981**, *16*, 1013.

**Table 1.** The Chemical Titration Results and Crystallographic Data for the Iridium Perovskite Oxide Samples Prepared in This Study

| compds | oxidation state of iridium | crystal system | unit cell parameters |
|---|---|---|---|
| $Ba_2SrIrO_6$ | 5.88 | rhombohedral | $a = 5.025$ Å, $\alpha = 60.48°$ |
| $Ba_2CaIrO_6$ | 6.00 | cubic | $a = 8.364$ Å |
| $Ba_2ZnIrO_6$ | 5.96 | cubic | $a = 8.103$ Å |
| $BaLaLiIrO_6$ | 5.98 | cubic | $a = 7.947$ Å |
| $Sr_2CaIrO_6$ | 5.98 | monoclinic | $a = 5.783$ Å, $b = 5.828$ Å, $c = 8.199$ Å, $\beta = 90.26°$ |
| $Sr_2MgIrO_6$ | 5.81 | cubic | $a = 7.891$ Å |
| $Ba_2YIrO_6$ | 4.98 | cubic | $a = 8.355$ Å |
| $La_2LiIrO_6$ | 4.99 | orthorhombic | $a = 5.635$ Å, $b = 5.556$ Å, $c = 7.869$ Å |
| $La_2MgIrO_6$ | 4.00 | orthorhombic | $a = 5.629$ Å, $b = 5.591$ Å, $c = 7.914$ Å |
| $La_2ZnIrO_6$ | 4.01 | orthorhombic | $a = 5.532$ Å, $b = 5.572$ Å, $c = 7.842$ Å |
| $SrIrO_3$ | 3.99 | orthorhombic | $a = 5.598$ Å, $b = 5.580$ Å, $c = 7.750$ Å |

$MgIrO_6$ because it is not soluble in weak acidic solutions. The results of the chemical titration are represented in Table 1.

**Crystallographic Analysis.** The X-ray powder diffraction data were obtained at room temperature with a Philips PW1050 spectrogoniometer using Cu Kα radiation with a graphite diffracted-beam monochromator. Experimental diffraction line angles were corrected using Si as an internal standard ($a_0 = 5.4305$ Å at 25 °C).

**Magnetic Susceptibility Measurement.** Magnetic susceptibilities were measured with an automatic DSM 8 type susceptometer in the range 4−800 K, with a magnetic field of 1.8 T. The equipment was calibrated using a single crystal of $Gd_2(SO_4)_3 \cdot 8H_2O$ for the low-temperature region and a single crystal of $Gd_2O_3$ for the high-temperature region.

**X-ray Absorption Measurements.** The X-ray absorption measurements on the Ir $L_{III}$-edge were carried out with synchrotron radiation by using the EXAFS facilities installed at the beam line 10B of the Photon Factory, the National Laboratory for High Energy Physics (Tsukuba, Japan), operated at 2.5 GeV, 260−370 mA. Samples were ground to fine powders in a mortar with Nujol as a diluent and then spread uniformly onto an adhesive tape, which was folded into several layers to obtain an optimum absorption jump ($\Delta\mu t \approx 1$) large enough to be free from the thickness and pin-hole effects.[20,48] All data were recorded with a spacing of ~0.4 eV for the XANES region and ~1.5 eV for the EXAFS region in the transmission mode at room temperature, using a Si(311) channel-cut monochromator. To ensure the reliability of the spectra, much care has been taken to evaluate the stability of the energy scale by monitoring the spectra of Ir metal for each measurement and thus edge positions were reproducible to better than 0.05 eV.

**XANES and EXAFS Data Analyses.** The data analysis for experimental spectra was performed by the standard procedure as follows.[49−51] The inherent background in the data was removed by fitting a polynomial to the pre-edge regioin and extrapolated through the entire spectrum, from which it was subtracted. The resulting spectra, $\mu(E)$, were normalized to an edge jump of unity for comparing the XANES features directly with one another. The absorption spectrum for the isolated atom, $\mu_0(E)$, was approximated by the sum of the cubic spline. The EXAFS function, $\chi(E)$, was obtained as $\chi(E) = \{\mu(E) - \mu_0(E)\}/\mu_0(E)$.

Further analysis was performed in $k$ space, where the photoelectron wave vector $k$ is defined as $k = \{(2m/\hbar^2)(E - E_0)\}^{1/2}$, where $m$ is the electron mass and $E_0$ is the threshold energy of the photoelectron at $k = 0$. The resulting EXAFS spectra were $k^3$ weighted and Fourier transformed in the range of ~3 Å$^{-1}$ ≤ $k$ ≤ ~14 Å$^{-1}$ with a Hanning apodization function. In order to determine the structural parameters of the Ir−O bond, a nonlinear least-squares curve fitting procedure was carried out for the inverse Fourier transformed $k^3\chi(k)$ of the first shell corresponding to the Ir−O bonding pair in the Fourier transform (FT) by using the EXAFS formula on the basis of the plane wave single-scattering description, which can be expressed as follows:

$$\chi(k) = -S_0^2 \sum_i \frac{N_i}{kR_i^2} F_i(k) \exp\{-2\sigma_i^2 k^2\} \exp\{-2R_i/\lambda(k)\} \sin\{2kR_i + \phi_i(k)\}$$

The back-scattering amplitude, $F_i(k)$, the total phase shift, $\phi_i(k)$, and the photoelectron mean free path, $\lambda(k)$, were theoretically calculated by the curved wave *ab initio* EXAFS code FEFF 5,[52] where the amplitude reduction factor and the Debye−Waller factor were set equal to unity and zero, respectively. The experimental threshold energy was located at 10 eV above the white line maximum. In the course of nonlinear least-squares curve fitting between the experimental $k^3\chi(k)$ and theory, the structural parameters such as the Ir−O bond distance, $R_i$, the coordination number, $N_i$, the Debye−Waller factor, $\sigma_i^2$, which represents a mean-square relative displacement, and the threshold energy difference, $\Delta E_0$, were optimized as variables. The amplitude reduction factor, $S_0^2$, was set equal to unity for the entire course of the fitting procedure. The reliability of the fit is determined by the $F$ factor, $F = [\sum\{(\chi(k)_{exp} - \chi(k)_{fit})k^3\}^2/(N - 1)]^{1/2}$, where $\chi(k)_{exp}$, $\chi(k)_{fit}$, and $N$ represent the experimental EXAFS oscillation, the fitted oscillation, and the number of data points, respectively.

## Results and Discussion

In our previous study[1] on the Ir $L_{III}$-edge XANES of three iridium oxides, we could successfully determine the electronic structure and the bonding character such as covalency as well as the local site symmetry because the $L_{III}$-edge XANES are quite sensitive to the oxidation state, the spin state, and the crystal field effect. In order to derive a general rule for applying such a method to 5d elements, we intended to extend our study at first to a large number of iridium oxides. But chemically well-characterized systems are needed for achieving such a purpose. Therefore, the X-ray diffraction and magnetic susceptibility measurements were carried out in advance for confirming the purity, the crystal structure, and the oxidation state of the iridium in the present compounds.

**Crystallographic Analysis.** According to the X-ray powder diffraction patterns, all the compounds prepared are found to have a perovskite-type structure. The $A_2BB'O_6$-type compounds show the superstructure resulting from the alternating ordering of (B−O−B'), as shown in Figure 1 (this is the case for $Ba_2CaIrO_6$). However, no evidence was detected for the A-site ordering of Ba−O−La in $BaLaLiIrO_6$[40] though it shows a Li/Ir superstructure. It is generally considered that the superstructure can be induced by the lattice energy stabilization due to

(46) Longe, J. M.; Kafalas, J. A.; Arnott, R. J. *J. Solid State Chem.* **1971**, *3*, 174.
(47) Chamberland, B. L.; Philpotts, A. R. *J. Alloys Compd.* **1992**, *182*, 355.
(48) Stern, E. A.; Kim, K. *Phys. Rev. B* **1981**, *23*, 3781.
(49) Teo, B. K. *EXAFS: Basic Principles and Data Analysis*; Springer-Verlag: Berlin, 1986.
(50) Sayers, D. E.; Bunker, B. A. In *X-ray Absorption: Principles, Applications, Techniques of EXAFS, SEXAFS, and XANES*; Koningsberger, D. C., Prins, R., Eds.; Wiley-Interscience: New York, 1988; p 211−253.
(51) Lytle, F. W. In *Applications of Synchrotron Radiation*; Winick, H., et al., Eds.; Gordon and Breach Science Publishers: New York, 1989; pp 135−223.
(52) Rehr, J. J.; Mustre de Leon, J.; Zabinsky, S. I.; Albers, R. C. *J. Am. Chem. Soc.* **1991**, *113*, 5135. Mustre de Leon, J.; Rehr, J. J.; Zabinsky, S. I. *Phys. Rev. B* **1991**, *44*, 4146. O'Day, P. A.; Rehr, J. J.; Zabinsky, S. I.; Brown, G. E., Jr. *J. Am. Chem. Soc.* **1994**, *116*, 2938.

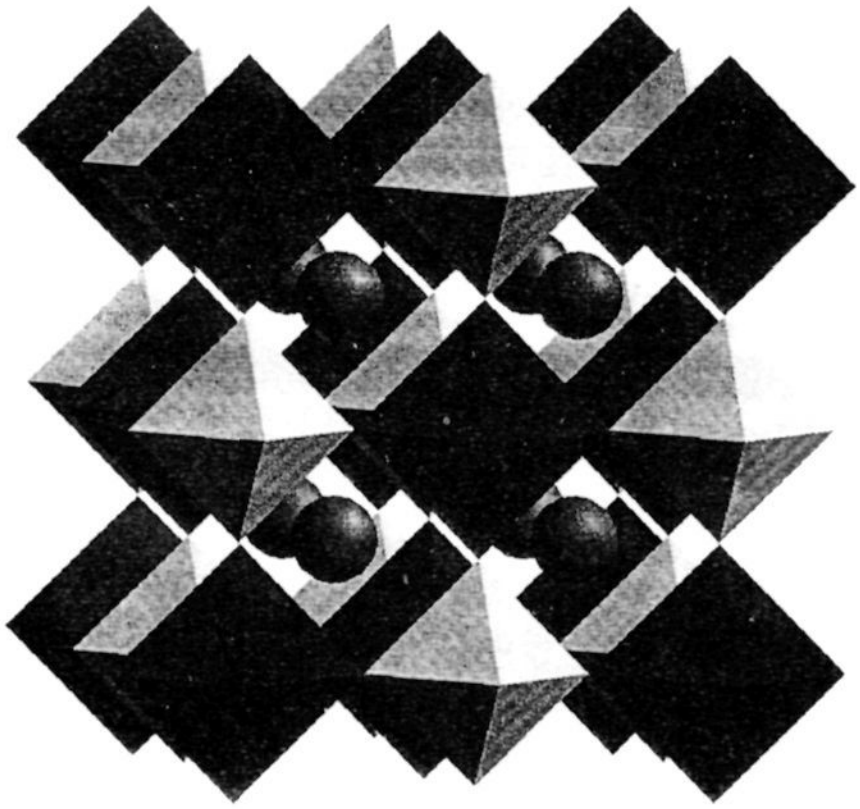

**Figure 1.** Ordered cubic perovskite structure of $Ba_2CaIrO_6$. Spheres, large octahedra, and small octahedra indicate Ba, $CaO_6$, and $IrO_6$, respectively.

the size and charge differences of two cations. The stabilization of electrostatic energy is induced by the B-site ordering rather than the A-site ordering because the B−O bonding in $BO_6$ octahedra competes directly with the B′−O bonding along the B−O−B′ directions. Unit cell parameters were calculated by the least-squares analysis of the X-ray powder diffraction data, which are given in Table 1.

**Magnetic Property.** It was found that all iridiums in these perovskites are stabilized with the low-spin $5d^n$ ($n = 3$, 4, and 5) state due to the strong crystal field for the 5d elements. The energy levels for the low-spin $5d^n$ ($n = 3$, 4, and 5) state in octahedral sites are usually deduced from the intermediate coupling scheme due to the strong spin−orbit coupling comparable to the Coulomb repulsion.[53,54]

The $d^3$ electronic configuration of $Ir^{VI}$ is characterized by a $^4A_{2g}$ ground term independent of the coupling scheme and the crystal field strength. The half-filled orbitals interact with each other to induce antiferromagnetic coupling at the low-temperature domain. Such a magnetic interaction in the ordered perovskite could be explained by the super−super exchange through oxygen p orbitals,[27] which is improved if the Ir−Ir distance becomes shorter (in the $Ir^{VI}$ compounds, the nearest $Ir^{VI}$−$Ir^{VI}$ distance is only 5.5−6.1 Å). Therefore a trend in the antiferromagnetic transition temperatures could be observed with respect to the nearest $Ir^{VI}$−$Ir^{VI}$ distances. The electronic configuration ($^4A_{2g}$) of $Ir^{VI}$ is expected to lead to a smaller moment than that corresponding to the spin-only value because only the second-order orbital contribution might be involved ($\mu_{cff} = \mu_{s.o.}(1 - 4\lambda/10Dq)$, where $\mu_{s.o.}$ is the spin-only value and $\lambda$ is spin-orbit coupling constant) and d orbitals are less than half filled. But the experimetnal magnetic moments approach the spin-only value due to the large crystal field strength corresponding to $Ir^{VI}$, inducing a small value for the $4\lambda/10Dq$ term. All $Ir^{VI}$ oxides follow the Curie−Weiss law in the paramagnetic domain and their molar magnetic moments are given in Table 2. The effective magnetic moments calculated from the molar Curie constants are dependent upon the oxygen contents of samples and the ionicities of B−O bonds in the $A_2BIrO_6$ (A = Ba, Sr, and La; B = Sr, Ca, Y, Zn, Mg, and Li) perovskites. The Néel temperature also might be influenced by the covalency of the $Ir^{VI}$−O bond as well as the structural distortion.

**Table 2.** Néel Temperatures ($T_N$), Effective Magnetic Moments ($\mu_{eff}$), and Weiss Constants ($\theta_p$) for $Ir^{VI}$ Compounds

| compd | $T_N$ (K) | $\mu_{eff}(\mu_B)^a$ | $\theta_p$ (K) |
|---|---|---|---|
| $Ba_2SrIrO_6$ | 45 | 3.64 | −365 |
| $Ba_2CaIrO_6$ | 55 | 3.90 | −573 |
| $Ba_2ZnIrO_6$ | 55 | 3.06 | −365 |
| $Sr_2CaIrO_6$ | 55 | 3.66 | −375 |
| $Sr_2ZnIrO_6$ | 45 | 2.99 | −271 |
| $Sr_2MgIrO_6$ | 80 | 3.11 | −724 |
| $BaLaLiIrO_6$ | − | 3.03 | −361 |

$^a$ $\mu_{eff}(\mu_B) = 2.84\sqrt{C_M}$, where $C_M$ is molar Curie constant in the paramagnetic temperature domain.

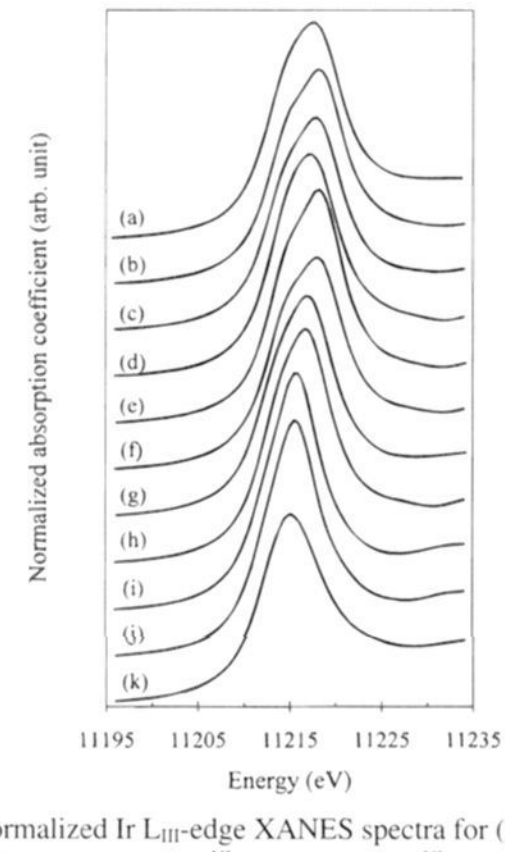


**Figure 2.** Normalized Ir $L_{III}$-edge XANES spectra for (a) $Sr_2MgIr^{VI}O_6$, (b) $Sr_2CaIr^{VI}O_6$, (c) $BaLaMgIr^{VI}O_6$, (d) $Ba_2ZnIr^{VI}O_6$, (e) $Ba_2CaIr^{VI}O_6$, (f) $Ba_2SrIr^{VI}O_6$, (g) $La_2LiIr^{V}O_6$, (h) $Ba_2YIr^{V}O_6$, (i) $La_2MgIr^{IV}O_6$, (j) $La_2ZnIr^{IV}O_6$, and (k) $SrIr^{IV}O_3$. The white line shift and the increase of shoulder in the lower energy part of the white line are shown as the oxidation state of the iridium increases.

Due to the strong crystal field in the 5d series, it is expected that $Ir^V$ ($La_2LiIrO_6$ and $Ba_2YIrO_6$) and $Ir^{IV}$ ($La_2MgIrO_6$, $La_2ZnIrO_6$, and $SrIrO_3$) exhibit the low-spin configurations $t_{2g}^4e_g^0$ and $t_{2g}^5e_g^0$, respectively. The ground term with $^3T_{1g}$ for $Ir^V$ with a large spin−orbit coupling constant ($\lambda \approx 3500$ cm$^{-1}$) has been calculated for $La_2LiIrO_6$ using the modified Kotani theory.[45] Also $Ir^{IV}$ induces a large $10Dq$ value, and the $^2T_{2g}$ ground term leads to a small deviation of magnetic susceptibility from the Curie−Weiss behavior.[42] On the contrary, for $SrIrO_3$ a Pauli paramagnetism with metallic conductivity[46,47] is observed due to the delocalization of the $5d^5$ electron via the Ir 5d−O 2p−Ir 5d bond sequence.

**Ir $L_{III}$-Edge XANES.** Figure 2 shows the Ir $L_{III}$-edge XANES spectra of the present perovskite compounds, in which the iridium ions with various oxidation states such as +IV, +V, and +VI are stabilized in an octahedral site. It is clearly seen that the peak positions shift to higher energies and the lower energy feature becomes better separated as the oxidation state of the iridium ion increases. In order to obtain the detailed structure at $L_{III}$-edges, the second-derivative curves of Figure 3 were obtained by using an interpolatory cubic spline derivative

(53) Moffitt, W.; Goodman, G. L.; Fred, M.; Weinstock, B. *Mol. Phys.* **1959**, *2*, 109.
(54) Kamimura, H. K.; Koide, S.; Sekiyama, H.; Sugano, S. *J. Phys. Soc. Jpn.* **1960**, *15*, 1264.

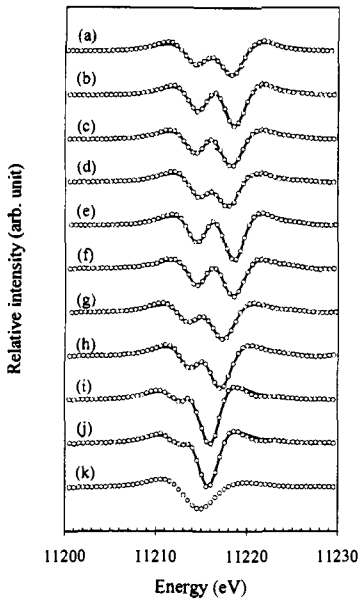


**Figure 3.** The second derivatives (open circles) of the Ir $L_{III}$-edge XANES spectra and the best fits (solid lines) by the sum of two Lorentzian functions to the second derivatives for (a) $Sr_2MgIr^{VI}O_6$, (b) $Sr_2CaIr^{VI}O_6$, (c) $BaLaMgIr^{VI}O_6$, (d) $Ba_2ZnIr^{VI}O_6$, (e) $Ba_2CaIr^{VI}O_6$, (f) $Ba_2SrIr^{VI}O_6$, (g) $La_2LiIr^{V}O_6$, (h) $Ba_2YIr^{V}O_6$, (i) $La_2MgIr^{IV}O_6$, (j) $La_2ZnIr^{IV}O_6$, and (k) $SrIr^{IV}O_3$.

evaluator and data smoother.[1] The second derivative spectra show more clearly the transitions to bound states, since the amplitude corresponding to the transitions to continuum states, described as an arctangent function, becomes almost negligible.[55] The white lines of all spectra except for $SrIrO_3$ consist of the double-peak that corresponds to the transitions to $t_{2g}$ and $e_g$ orbitals, respectively, reflecting the local site symmetry around the iridium ions to be a nearly regular octahedron.[1,2,19,21] Moreover the peak intensity corresponding to the transition to $e_g$ orbitals in the higher energy is almost the same, whereas that to $t_{2g}$ orbitals in the lower energy side increases as the iridium ions have higher oxidation states, which implies that all iridium ions are in the low-spin state as expected for most third-row transition-metal ions. But the second derivative of $SrIrO_3$ shows only a broad peak without splitting, which is the same as $IrO_2$, as previously reported.[1,9,56] We have suggested that the lack of splitting might be due to the $IrO_6$ octahedra being structurally coupled with one another, this being different from the B-site-ordered perovskite. And these coupled octahedra, which could be regarded no longer as a single cluster of $[IrO_6]^{8-}$, might certainly contribute to the lack of splitting of the white line in that the $IrO_6$ octahedra for $SrIrO_3$ are also linked by sharing vertices of one another to form a 3D structure. It should be noted that coupled octahedra are not a prerequisite for no splitting of the white line. For example, $WO_2$ and $ReO_2$ crystallize with a rutile structure as $IrO_2$, but they show weak splitting of the $L_{III}$-edge white line. This implies that the degree of vacancy in unoccupied states influences the splitting of the white line.

To get quantitative results for the two peaks corresponding to the $t_{2g}$ and $e_g$ states in the second derivatives, a least-squares fitting of a sum of two Lorentzian curves to the second-derivative spectra was carried out. As mentioned before, the spectral shape in the second-derivative spectra can be described only as the Lorentzian functions corresponding to the transitions to bound states. The major component of the second derivative of a positive Lorentzian is a narrow, symmetrical, negative-direction peak that maintains the same relative intensity and position as the original Lorentzian. The has an advantage in that the number of parameters in the fitting procedure is reduced by excluding contribution due to the transition to the continuum state and so we get a physically meaningful evolution in the edge spectral features. This fitting procedure to the second-derivative spectra has been extensively used for its simplicity and accuracy compared to the raw spectra.[1,21,55] The best-fitting results are compared with the experimental spectra in Figure 3 and listed in Table 3. The three previously reported compounds[1] $La_2MgIr^{IV}O_6$, $La_2LiIr^{V}O_6$, and $Ba_2CaIr^{VI}O_6$ were remeasured for the purpose of an exact comparison with the other ones and the present fitting results for these compounds show a good reproducibility again with respect to the previous ones. Figure 4 exhibits the evolution of the oxidation state of the iridium versus the average energy position corresponding to transitions to the $t_{2g}$ and $e_g$ states, in which the error bar represents the spread of energy positions. It is clearly seen that the peak positions shift to higher energies with an increase in the oxidation state of the iridium ions, and the easier susceptibility of the crystal field of $e_g$ states oriented directly to ligands in $O_h$ symmetry results in a larger change of peak position corresponding to transition to $e_g$ states than that to $t_{2g}$ states. These facts observed for a larger number of iridium compounds again support the previous results very well. In addition, the spread of energy positions as denoted by the error bar is much larger for transition to $e_g$ states than to $t_{2g}$ states, and it is also larger for the iridium with the higher oxidation state. In particular, the latter implies that the chemical bonding character around the iridium could be more significantly influenced by the change of chemical environments as the oxidation state of the iridium increases. That is, in the perovskite compounds with the general formula $A_2BIrO_6$, the Ir−O bond competes with the B−O and A−O bonds by sharing the same oxygen 2p orbitals via a pathway of 180° and 90°, respectively. Therefore the Ir−O bonding character such as covalency would be influenced by the nature of atoms A and B. We can determine a tentative conclusion that the transition-metal ion with a high oxidation state would be more preferable for inducing a variety of physicochemical properties through the change in chemical environments.

Now it is very important to examine quantitatively how the oxidation state of the iridium and the nature of atoms A and B act on the crystal field of the iridium site in the perovskite lattice of $A_2BIrO_6$, which represents the degree of covalency of the Ir−O bond. Strictly speaking, the energy splitting in the white line of the $L_{III}$-edge XANES spectra is not equal to the crystal field parameter, $10Dq$, because any transition in the $L_{III}$-edge XANES spectra occurs from a $d^n$ ground state to a $p^5d^{n+1}$ final state.[10,19,21] Unfortunately it is very difficult to obtain directly the crystal field strength from the optical spectroscopic method for the perovskite compounds because d−d transitions are

(55) Lytle, F. W.; Greegor, R. B. *Appl. Phys. Lett.* **1990**, *56*, 192.

(56) Horsley suggested in ref 9 that some of the unoccupied d states in $IrO_2$ might be measured by the resonance transition because $IrO_2$ has significantly less ionic character. But even though the B-site ordered perovskites, $La_2MgIrO_6$ and $La_2ZnIrO_6$, have more covalent bonding character in the Ir−O bond than $IrO_2$ and $SrIrO_3$ because of the presence of ionic competing bonds such as Mg−O and Zn−O (see text), the ordered perovskites show transitions to both $t_{2g}$ and $e_g$ states. In addition, Sham has calculated the transition intensities using the wave functions of $Ru^{III}$ ($d^5$) in a cubic strong crystal field case (ref 10) to show the presence of transition to the $t_{2g}$ state in the $L_{III}$-edge spectrum. Thus he suggested that the consideration of local geometry (tetragonal symmetry) in $IrO_2$ might predict the absence of transition to the $t_{2g}$ state. But $SrIrO_3$, in which the $Ir^{IV}$ ion has the same electronic configuration ($d^5$) and cubic local geometry as the above $Ru^{III}$ compound, also exhibits no transition to the $t_{2g}$ state, contrary to the expectation. This fact implies that the calculation based on the single cluster orbital model of $[IrO_6]^{8-}$ might be difficult to apply for a system where octahedra are strongly coupled with one another.

**Table 3.** Lorentzian-Fitting Parameters ($E$, $H$, and $\Gamma$) and Peak Area ($A$) of the Second Derivatives of the Ir $L_{III}$-Edge XANES Spectra[a]

| compd | position ($E$/eV) | | height ($H$) | | fwhm ($\Gamma$/eV) | | area ($A$/eV) | |
|---|---|---|---|---|---|---|---|---|
| | $E_{t_{2g}}$ | $E_{e_g}$ | $H_{t_{2g}}$ | $H_{e_g}$ | $\Gamma_{t_{2g}}$ | $\Gamma_{e_g}$ | $A_{t_{2g}}$ | $A_{e_g}$ |
| $La_2ZnIrO_6$ | 11212.65 ± 0.02 | 11215.70 ± 0.01 | 0.61 ± 0.02 | 2.57 ± 0.03 | 2.78 ± 0.05 | 3.07 ± 0.02 | 3.4 ± 0.1 | 15.8 ± 0.2 |
| $La_2MgIrO_6$ | 11212.66 ± 0.02 | 11215.84 ± 0.01 | 0.64 ± 0.02 | 2.68 ± 0.04 | 2.82 ± 0.07 | 3.07 ± 0.02 | 3.6 ± 0.2 | 16.5 ± 0.3 |
| $La_2LiIrO_6$ | 11213.60 ± 0.01 | 11217.27 ± 0.01 | 1.10 ± 0.03 | 2.41 ± 0.02 | 3.21 ± 0.04 | 3.63 ± 0.01 | 7.1 ± 0.2 | 17.5 ± 0.1 |
| $Ba_2YIrO_6$ | 11213.77 ± 0.02 | 11217.03 ± 0.01 | 1.25 ± 0.03 | 2.44 ± 0.05 | 3.06 ± 0.03 | 3.30 ± 0.03 | 7.7 ± 0.2 | 16.1 ± 0.4 |
| $Sr_2MgIrO_6$ | 11214.49 ± 0.01 | 11218.20 ± 0.01 | 1.47 ± 0.03 | 2.18 ± 0.01 | 3.51 ± 0.04 | 3.62 ± 0.01 | 10.3 ± 0.2 | 15.8 ± 0.1 |
| $Sr_2CaIrO_6$ | 11214.62 ± 0.01 | 11218.52 ± 0.01 | 1.34 ± 0.03 | 2.17 ± 0.03 | 3.08 ± 0.03 | 3.22 ± 0.01 | 8.2 ± 0.2 | 14.0 ± 0.2 |
| $BaLaLiIrO_6$ | 11214.33 ± 0.01 | 11218.18 ± 0.01 | 1.23 ± 0.02 | 2.21 ± 0.02 | 3.10 ± 0.03 | 3.43 ± 0.01 | 7.6 ± 0.1 | 15.2 ± 0.1 |
| $Ba_2ZnIrO_6$ | 11214.62 ± 0.01 | 11217.78 ± 0.01 | 1.24 ± 0.02 | 2.15 ± 0.03 | 3.05 ± 0.02 | 3.48 ± 0.03 | 7.6 ± 0.1 | 15.0 ± 0.3 |
| $Ba_2CaIrO_6$ | 11214.59 ± 0.01 | 11218.48 ± 0.01 | 1.41 ± 0.06 | 2.43 ± 0.07 | 2.98 ± 0.06 | 3.17 ± 0.05 | 8.4 ± 0.4 | 15.4 ± 0.5 |
| $Ba_2SrIrO_6$ | 11214.48 ± 0.01 | 11218.36 ± 0.01 | 1.30 ± 0.02 | 2.15 ± 0.02 | 3.02 ± 0.03 | 3.36 ± 0.02 | 7.9 ± 0.2 | 14.5 ± 0.1 |

[a] The fitting function if $L(\epsilon) = H\Gamma^2/\{(\epsilon - E)^2 + \Gamma^2\}$, where $E$, $H$, and $\Gamma$ refer to energy position, height, and full width at half maximum (fwhm) of the peak, respectively.

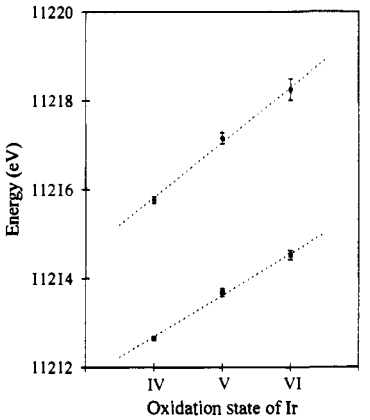


**Figure 4.** Plots of the average energy position corresponding to transitions to $t_{2g}$ (■) and $e_g$ states (●) versus the oxidation state of the iridium in the perovskite compounds. Linear chemical shifts of transition energies with an increase in the oxidation state are shown. The spread of energy positions is significantly larger for transition to $e_g$ states than to $t_{2g}$ states, and larger for the higher oxidation state.

overlaid by intense ligand-to-metal charge transfer (LMCT) transition in most cases, and moreover the prepared iridium oxides are not transparent in the ultraviolet and visible regions. For these reasons, the B′−O bond covalency in the $A_2BB'O_6$ perovskite compounds has been qualitatively estimated by examining the ionicities of the A−O and B−O bonds which compete with the B′−O bond as stated above.[27-34] The ionicity (I) of the a−b bond is defined by Pauling's formula as follows,[57]

$$I = 1 - \exp[-(\chi_a - \chi_b)^2/4]$$

where $\chi_a$ and $\chi_b$ indicate the electronegativities of atoms a and b, respectively. Pauling's ionicities of the A−O and B−O bonds in the present compounds of $A_2BIrO_6$ (A = Ba, Sr, and La; B = Sr, Ca, Y, Zn, Mg, and Li) were calculated by using both Pauling's[58] and Allred−Rochow's[58,59] electronegativities as shown in Table 4. Two methods using different electronegativities show Pauling's ionicity in the same order of Ba−O > Sr−O > Ca−O > La−O > Y−O > Mg−O > Zn−O except for the Li−O bond. Therefore, the Ir−O bond covalency has been expected to increase as Pauling's ionicities of the competing A−O and B−O bonds increase. The role of an inductive effect resulting from the covalent character of A−X (A = cation, X = anion in the lattice) in solid state chemistry has been recently underlined and applied to various experimental results.[60] Therefore, it is of great interest to examine the correlation between the bond covalency and the crystal field strength.

**Table 4.** Ionic Radii of Six- or Twelve-Coordinated Metal Ions[a] and Pauling's Ionicities[b] for the Chemical Bond between Metal and Oxygen

| chemical bond | ionic radius of metal ion (Å) | Pauling's ionicity | |
|---|---|---|---|
| | | $A^c$ | $B^d$ |
| $Ba^{II}-O^{-II}$ | 1.61 (C.N. = 12), 1.35 (C.N. = 6) | 0.803 | 0.798 |
| $Sr^{II}-O^{-II}$ | 1.44 (C.N. = 12), 1.18 (C.N. = 6) | 0.787 | 0.792 |
| $La^{III}-O^{-II}$ | 1.36 (C.N. = 12), 1.03 (C.N. = 6) | 0.745 | 0.768 |
| $Li^{-I}-O^{-II}$ | 0.76 (C.N. = 6) | 0.779 | 0.798 |
| $Ca^{II}-O^{-II}$ | 1.00 (C.N. = 6) | 0.774 | 0.779 |
| $Y^{III}-O^{-II}$ | 0.90 (C.N. = 6) | 0.708 | 0.760 |
| $Mg^{II}-O^{-II}$ | 0.72 (C.N. = 6) | 0.678 | 0.724 |
| $Zn^{II}-O^{-II}$ | 0.74 (C.N. = 6) | 0.551 | 0.571 |

[a] From ref 66. [b] $I = 1 - \exp[-(\chi_a - \chi_b)^2/4]$, where $\chi_a$ and $\chi_b$ indicate the electronegativities of atoms a and b, respectively. [c] Ionicities calculated from Pauling's electronegativities. [d] Ionicities calculated from Allred−Rochow's electronegativities.

Turning to the $L_{III}$-edge XANES spectra, they are highly sensitive to the detail of the ground state, and they carry the signature of atomic terms involved in the ground state[18] such that the white line splitting can be given as a function of the crystal field parameter, $10Dq$,[10] even though the energy splitting is not equal to $10Dq$ as stated above. In this regard, $L_{III}$-edge XANES studies are very instructive since they can give us the quantitative information on the covalency of the metal−ligand bond. Figure 4 clearly shows that the average energy splitting between two peaks corresponding to transitions to $t_{2g}$ and $e_g$ states increases as the iridium ion is oxidized. This fact implies that the crystal field strength is dependent on the oxidation state of the metal as expected in the spectrochemical series.[31] In addition, for each oxidation state, it is necessary to compare the degree of covalency in the Ir−O bond upon the change of chemical environments such as atoms A and B in the present compounds, $A_2BIrO_6$, since the detailed changes in energy splittings are dominantly due to changes in the covalent character of Ir−O bonds although changes in electrostatic potential may also be at least partially responsible for the changes in energy splittings.

Comparing $La_2ZnIrO_6$ with $La_2MgIrO_6$, the only factor that influences the Ir−O bond covalency is the different B cations, Zn and Mg, because both compounds have the same A cation (La) and the same iridium oxidation state. According to Pauling's ionicities for Zn−O and Mg−O bonds in Table 4, the Ir−O bond covalency in $La_2MgIrO_6$ might be expected to

(57) Pauling, L. *The Nature of the Chemical Bond*, 3rd ed.; Cornell University: New York, 1972; p 98.
(58) Huheey, J. E. *Inorganic Chemistry: Principles of Structure and Reactivity*, 3rd ed.; Harper and Row: New York, 1983; p 146.
(59) Allred, A. L.; Rochow, D. E. G. *J. Inorg. Nucl. Chem.* **1968**, *5*, 264.
(60) Etourneau, J.; Portier, J.; Menil, F. *J. Alloys Compd.* **1992**, *188*, 1.

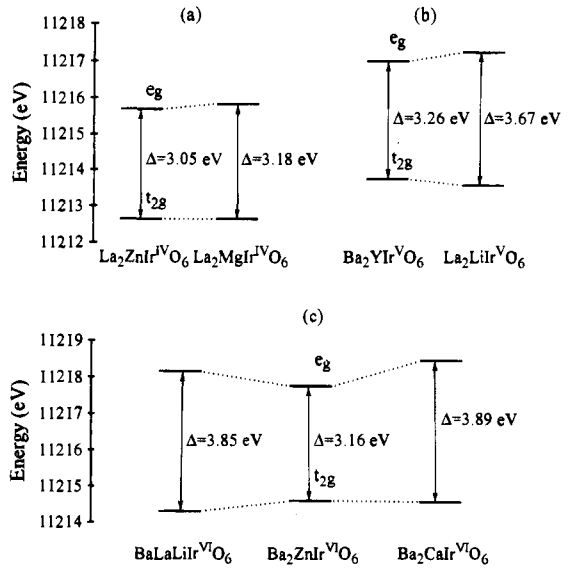


**Figure 5.** Schematic illustration of the relative transition energies and the energy splittings for (a) $La_2ZnIrO_6$ and $La_2MgIrO_6$, (b) $Ba_2YIrO_6$ and $La_2LiIrO_6$, and (c) $BaLaLiIrO_6$, $Ba_2ZnIrO_6$, and $Ba_2CaIrO_6$. We can see the influence of the nature of atoms A and B on the crystal field of the iridium site in the perovskite lattice.

be larger than that in $La_2ZnIrO_6$. In fact, the energy positions and the splittings of the $L_{III}$-edge spectra also show that the stronger crystal field due to the enhanced Ir−O bond covalency acts on the iridium of $La_2MgIrO_6$ as shown schematically in Figure 5a. These results quantitatively support the above expectation of the bonding character through Pauling's ionicity well. Figure 5b presents a comparison of relative transition energy positions and the splittings for $La_2LiIrO_6$ and $Ba_2YIrO_6$ for $Ir^V$ compounds, where the Ir−O bond covalency in $La_2LiIrO_6$ is much larger than that in $Ba_2YIrO_6$. Even though the ionicity of the Li−O bond in Table 4 shows a different order in a series of ionicities for various M−O bonds when using Pauling's and Allred-Rochow's electronegativities, respectively, its ionicity is always larger than that of the Y−O bond in $Ba_2YIrO_6$. It is therefore expected from the consideration of ionicities for Li−O and Y−O bonds that the Ir−O bond in $La_2LiIrO_6$ will be more covalent than that in $Ba_2YIrO_6$. On the other hand, the ionicity of the La−O bond in $La_2LiIrO_6$ is smaller than that of the Ba−O bond in $Ba_2YIrO_6$. Now the influence of the competing bond in site A (La−O and Ba−O) on the crystal field of $Ir^V$ through $\pi$- and $\sigma$-bonding with the oxygen 2p orbital should be considered in this comparison.[30] Though the energy contribution of cation A is usually less efficient than that of cation B, the crystal field of the iridium is significantly influenced by the volume contraction of the octahedral site from the size and the electronegativity of cation A. The smaller size of cation A allows a smaller space for cation B in the octahedral site, resulting in a stronger crystal field ($\Delta$cc) on the B site for the short $Ir^V$−O distance and the strong destabilization ($\Delta\sigma$) of the $\sigma(e_g(Ir^V)-2p(O))$ bond. At the same time the $\sigma$(La−O) bond becomes more covalent than the $\sigma$(Ba−O) bond, which induces smaller destabilization ($\Delta\pi$) of the lower $t_{2g}$ level. Finally we can represent the crystal field strength approximately as follows,

$$10Dq = \Delta cc + \Delta\sigma - \Delta\pi$$

This qualitative consideration of the bonding character and the crystal field energy gives us the conclusion that $La_2LiIrO_6$ shows much higher $\Delta E$ than $Ba_2YIrO_6$ from the XANES results. The crystal field strength at the iridium site in $La_2LiIrO_6$ ($\Delta E$ = 3.67 eV) exhibits almost the comparable order to the average value ($\Delta E$ = 3.73 eV) of the $Ir^{VI}$ compounds. The reasons for such a large $\Delta E$ in $La_2LiIrO_6$ can be explained by several factors that favor the large crystal field strength. $La_2LiIrO_6$ has a very weak competing bond in site B (less covalent Li−O bond) and the small A cation (La) induces a stronger covalent $\sigma$(La−O) bond than a Ba−O bond. Consequently, the Ir−O bond covalency in $A_2BIrO_6$ might be influenced by the size and electronegativity of cation $A^{30}$ and mainly the ionicity of the B−O bond, as well as by the oxidation state of the iridium.

The above relationship between the Ir−O bond covalency and the chemical environments also can be applied to the $Ir^{VI}$ compounds. Comparing three compounds containing the Ba ion as the A cation, $Ba_2ZnIrO_6$, $Ba_2CaIrO_6$, and $Ba_2SrIrO_6$, shows energy splittings of 3.16, 3.89, and 3.88 eV, respectively, in which $Ba_2ZnIrO_6$ shows much smaller $\Delta E$ due to the covalent Zn−O bond as shown in Figure 5c. The expectation through ionicities of the competing B−O bonds is in good agreement with the present Ir $L_{III}$-edge XANES results. Because $\Delta E$ for $Ba_2CaIrO_6$ is close to that for $Sr_2CaIrO_6$, it is suggested that the crystal field strength ($10Dq$) is predominantly determined by the high oxidation state (+VI) of the iridium, and the size effect of cation A is not comparable with the energy level splitting by the large difference of oxidation states ($Ir^{VI}$ and $O^{II-}$).

On the other hand, the Ir−O bond covalency in $Ba_2SrIrO_6$ deviates from our expectation due to the large ionicity of the Sr−O bond. The chemical titration of $Ba_2SrIrO_6$ revealed the average oxidation state of the iridium to be 5.88 rather than 6.00, as shown in Table 1. This means that overall about 12% of the iridium ions in $Ba_2SrIrO_6$ are in the $Ir^V$ state with the formation of oxygen vacancies.[39] Therefore the presence of $Ir^V$ and oxygen vacancies might induce the lower transition energies ($E_{t_{2g}}$ = 11214.48 eV, $E_{e_g}$ = 11218.36 eV) in $Ba_2SrIrO_6$, compared to the transition energies ($E_{t_{2g}}$ = 11214.56 eV, $E_{e_g}$ = 11218.48 eV) in $Ba_2CaIrO_6$. These effects also occur for $Sr_2MgIrO_6$. The average oxidation state of the iridium in $Sr_2MgIrO_6$ is 5.81, resulting in the presence of $Ir^V$ ions of about 19% and the corresponding oxygen vacancies. The relative transition energies and the energy splittings for $BaLaLiIrO_6$, $Ba_2ZnIrO_6$, and $Ba_2CaIrO_6$ are schematically shown in Figure 5c. In the present work, we have, for the first time, examined quantitatively the chemical effects on the covalency of the Ir−O bond in the various perovskite oxides by means of Ir $L_{III}$-edge XANES spectroscopy, which revealed that the qualitative expectation on the degree of covalency through Pauling's ionicity is still valid. Furthermore, the fact that the oxygen vacancy would significantly influence the metal−oxygen bond covalency could provide valuable information for studies of other compounds, in particular, nonstoichiometric systems.

It has been pointed out that the white line area in the $L_{III}$-edge spectrum does not necessarily represent the statistical vacancy of the unoccupied d states because of various factors that influence the peak area such as the thickness effect[51] of the broadening effect due to the spin-exchange interaction[10,21] and covalent bonding character,[19] but there is a good linear relationship between the difference in the areas for each transition state and the oxidation state of the iridium.[1,8,9] The present work for a large number of oxides provides good support for the above suggestion about the relationship between the white line and the charge as shown in Figure 6, which represents the plot for the average value of the differences, $\Delta A$ ($=A_{e_g} - A_{t_{2g}}$), between areas corresponding to transitions to $t_{2g}$ ($A_{t_{2g}}$) and $e_g$ states ($A_{e_g}$) versus the oxidation state of the iridium.

On the other hand, as the dipole-allowed transition for the

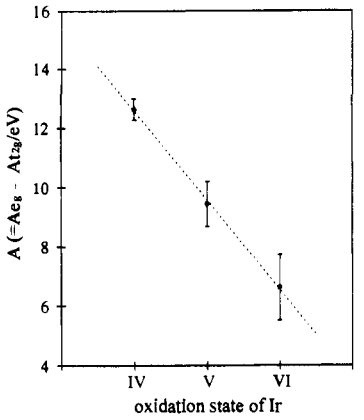


**Figure 6.** Plot of the average value of the differences, $\Delta A$ ($=A_{e_g} - A_{t_{2g}}$), between the white line areas corresponding to transitions to $e_g$ ($A_{e_g}$) and $t_{2g}$ ($A_{t_{2g}}$) versus the oxidation state of the iridium.

$L_{II}$-edge is $2p_{1/2}$ to $nd_{3/2}$, the $L_{II}$-edge XANES spectra are complementary to the $L_{III}$-edge spectra for which the dipole-allowed transitions are $2p_{3/2}$ to $nd_{3/2}$ and $nd_{5/2}$. Analyses of the $L_{II}$-edge XANES spectra for Ir perovskite compounds also will be carried out in further studies in order to obtain information on the effect of spin–orbit coupling by comparing the $L_{II}$- and $L_{III}$-edge XANES spectra.

**Ir $L_{III}$-edge EXAFS.** It is also of great interest to examine quantitatively the change of Ir–O bond distances with the change in oxidation states of the iridium ions. Although the metal–oxygen bond distance in the metal oxide system has been mainly obtained by the X-ray diffraction method so far, it is not easy to measure precisely the metal–oxygen bond distance because of the low X-ray scattering factor of oxygen as well as the anisotropic thermal effect due to the strong covalent bonding character. Therefore the determination of the metal–oxygen bond distance by means of EXAFS spectroscopy might be quite instructive because the first shell for the nearest neighbor of oxygen around the central metal is well separated from the other distant shells in materials such as perovskite compounds, despite the fact that it is difficult to determine the crystal system due to the short mean free path of photoelectrons.

The $k^3$-weighted Ir $L_{III}$-edge EXAFS spectra for the present perovskite compounds and their Fourier transforms (solid line) in the range of $\sim 3$ Å$^{-1} \leq k \leq \sim 14$ Å$^{-1}$ are shown in Figue 7. The first peak in the Fourier transforms is attributed to the Ir–O bonding pair, and its large intensity and high symmetry result from the undistorted octahedrally coordinated iridium, as expected from XANES spectra. The first shell of the Ir–O bond was isolated by inverse Fourier transform to $k$ space. The resulting $k^3\chi(k)$ filtered EXAFS oscillations are shown in Figure 8 (solid line) and the curve fittings were carried out to these EXAFS oscillations in order to determine the bond distance ($R$), the coordination number ($N$), and the Debye–Waller factor ($\sigma^2$). The best fitting results to the Fourier filtered first coordination shell are compared with the experimental spectra in Figures 7b and 8, and the fitted structural parameters are listed in Table 5. In the present compounds, the Ir–O bond was fitted to a single distance indicating that the local site symmetry of the iridium ions is regularly octahedral within experimental error.

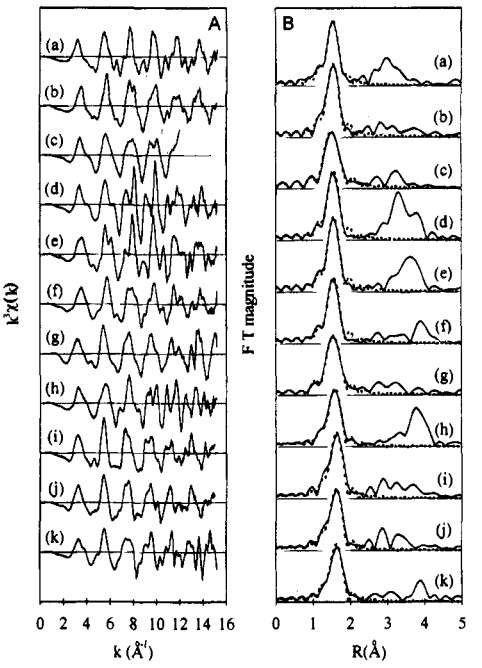


**Figure 7.** (a) The $k^3$-weighted Ir $L_{III}$-edge EXAFS spectra and (B) their Fourier transforms (solid line) for the $k$ range indicated in parentheses below and a best fit (dashed line) generated by using the Fourier filtered first shell corresponding to the Ir–O bonding pair in (a) $Sr_2MgIrO_6$ (2.8–14.2 Å$^{-1}$), (b) $Sr_2CaIrO_6$ (3.0–14.0 Å$^{-1}$), (c) $BaLaMgIrO_6$ (3.0–11.2 Å$^{-1}$), (d) $Ba_2ZnIrO_6$ (3.0–14.2 Å$^{-1}$), (e) $Ba_2CaIrO_6$ (3.0–14.1 Å$^{-1}$), (f) $Ba_2SrIrO_6$ (3.0–14.2 Å$^{-1}$), (g) $La_2LiIrO_6$ (2.7–14.0 Å$^{-1}$), (h) $Ba_2YIrO_6$ (2.9–14.2 Å$^{-1}$), (i) $La_2MgIrO_6$ (2.8–14.1 Å$^{-1}$), (j) $La_2ZnIrO_6$ (2.7–14.1 Å$^{-1}$), and (k) $SrIrO_3$ (2.8–14.2 Å$^{-1}$).

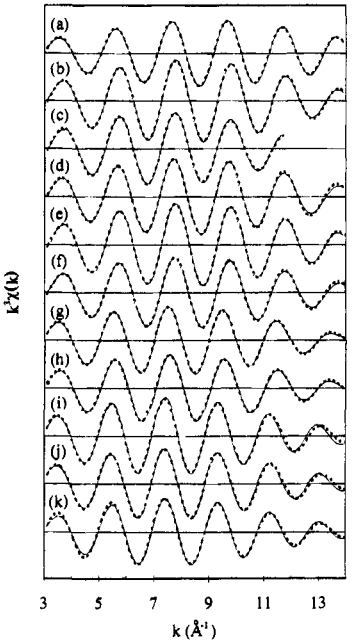


**Figure 8.** Fourier-filtered EXAFS spectra (solid line) arising from atoms in the first coordination sphere of the iridium in (a) $Sr_2MgIrO_6$, (b) $Sr_2CaIrO_6$, (c) $BaLaMgIrO_6$, (d) $Ba_2ZnIrO_6$, (e) $Ba_2CaIrO_6$, (f) $Ba_2SrIrO_6$, (g) $La_2LiIrO_6$, (h) $Ba_2YIrO_6$, (i) $La_2MgIrO_6$, (j) $La_2ZnIrO_6$, and (k) $SrIrO_3$. The best fit (dashed lines) were simulated by using the structural parameters of Table 5.

(61) A small discrepancy might be attributed to the difference between the present fitting method and the previous method, in which the latter used $Ir^{IV}O_2$ as a model compound. There are, in fact, some problems in using $Ir^{IV}O_2$ as a model compound for an analysis of the EXAFS spectrum. First, $Ir^{IV}O_2$ has two unresolvable Ir–O bond distances due to its rutile structure, which might result in the wrong structural parameters including amplitude function. Second, the atomic charge effect (ref 49) causes phase transferability but not to completion, though this effect can be partially compensated for by the variation of $\Delta E_0$. Third, analytical errors might be introduced by the background subtraction procedure for the experimental spectra of the unknown and model compounds (ref 52). Despite a difference between the applied fitting procedures, we can see that $La_2MgIr^{IV}O_6$ actually shows the same bond distance, which might be due to the same oxidation state of $Ir^{IV}$ and similar bond distances between unknown and model compounds.

**Table 5.** Bond Distance ($R$), Coordination Number ($N$), Debye−Waller Factor ($\sigma^2$), and Difference in Threshold Energy ($\Delta E_0$) Obtained from Nonlinear Least-Squares Curve Fits of Fourier Filtered First-Shell EXAFS Spectra Corresponding to the Ir−O Bonding Pair

| compd | oxidation state of Ir | $R$ (Å) | $N$ | $\sigma^2$ ($\times 10^{-3}$/Å$^2$) | $\Delta E_0$ (eV) | $F^a$ |
|---|---|---|---|---|---|---|
| $SiIrO_3$ | +4 | $2.00_5$ | 5.7 | 3.50 | −1.4 | 0.33 |
| $La_2MgIrO_6$ | +4 | $2.00_4$ | 6.3 | 3.30 | −1.5 | 0.38 |
| $La_2ZnIrO_6$ | +4 | $1.99_8$ | 6.0 | 3.33 | −2.1 | 0.29 |
| $La_2LiIrO_6$ | +5 | $1.95_9$ | 5.6 | 2.50 | −2.1 | 0.12 |
| $Ba_2YIrO_6$ | +5 | $1.96_2$ | 5.4 | 3.27 | −2.4 | 0.17 |
| $Sr_2MgIrO_6$ | +6 | $1.92_7$ | 5.3 | 1.91 | −2.9 | 0.14 |
| $Sr_2CaIrO_6$ | +6 | $1.92_2$ | 5.4 | 1.99 | −1.8 | 0.14 |
| $BaLaLiIrO_6$ | +6 | $1.92_0$ | 5.0 | 1.70 | −3.2 | 0.15 |
| $Ba_2ZnIrO_6$ | +6 | $1.93_0$ | 5.3 | 2.10 | −2.9 | 0.19 |
| $Ba_2CaIrO_6$ | +6 | $1.92_6$ | 5.2 | 1.76 | −1.8 | 0.10 |
| $Ba_2SrIrO_6$ | +6 | $1.92_8$ | 5.0 | 2.23 | −2.0 | 0.17 |

[a] $F$ indicates root-mean-square derivation between data and fit given by $F = \{\sum\{k^3(\chi(k)_{exp} - \chi(k)_{fit})\}^2/(N-1)\}^{1/2}$, where $N$ is the number of data points.

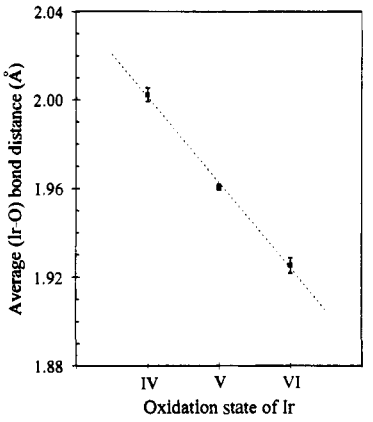


**Figure 9.** Variation of the average Ir−O bond distance upon the oxidation state ($N$) of iridium in the present compounds. Linear fit to the experimental data gives $d(Ir^N-O) = 2.155 - 0.039N$.

In Table 5, the Ir−O bond distances decrease depending upon the oxidation state of the iridium. But the Ir−O bond distances of 2.004, 1.959, and 1.926 Å for $La_2MgIr^{IV}O_6$, $La_2LiIr^{V}O_6$, and $Ba_2CaIr^{VI}O_6$, respectively, show only a small difference[61] from the previously reported values. The average bond distances for $Ir^{IV}$, $Ir^{V}$, and $Ir^{VI}$ are 2.002, 1.961, and 1.925 Å, respectively, which represents a good linearity to the oxidation states of the iridium as shown in Figure 9. Assuming the ionic radius of oxygen as the difference between the Ir−O bond distance and the ionic radii of six-coordinated $Ir^{IV}$ (0.625 Å) and $Ir^{V}$(0.57 Å) estimated by Shannon,[62] the ionic radii of oxygen consisting of the $Ir^{IV}$−O bond and the $Ir^{V}$−O bond are 1.377 and 1.391 Å, respectively, of which extrapolation gives the ionic radius of oxygen to be 1.404 Å in the case of the $Ir^{VI}$−O bond distance of 1.925 Å. Now the ionic radius of octahedrally coordinated $Ir^{VI}$ can be estimated as 0.521 Å from the difference between the experimental $Ir^{VI}$−O bond distance of 1.925 Å and the estimated ionic radius of oxygen of 1.404 Å. In order to examine the reliability of this method, the ionic radius of the $Ir^{III}$ ion was calculated from the oxygen radius (1.364 Å) estimated by the above method and the $Ir^{III}$−O bond distance (2.043 Å) obtained by the extrapolation of experimental $Ir^{IV}$−O, $Ir^{V}$−O, and $Ir^{VI}$−O bond distances. The resulting $Ir^{III}$ ionic radius of 0.676 Å is in excellent agreement with Shannon's ionic radius of octahedrally coordinated $Ir^{III}$ (0.68 Å).

(62) Shannon, R. D. *Acta Crystallogr. A* **1976**, *32*, 751.

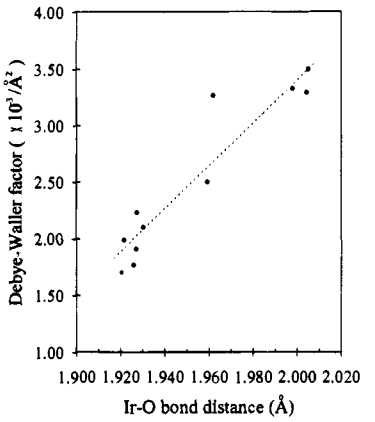


**Figure 10.** The relationship between the Debye−Waller factors and the Ir−O bond distances. A larger bond distance tends to exhibit a larger Debye−Waller factor ($\sigma^2$), which suggests that $\sigma^2$ might be mainly due to the thermal vibration of the Ir−O bond and thus there is no possibility of oxygen vacancy and multiple Ir−O bond distances resulting in the static disorder.

One of the important variables in the EXAFS analysis is the Debye−Waller factor, $\sigma^2$, which corresponds to the mean square relative displacement (MSRD) of the equilibrium of the Ir−O bond distance due to the vibration and/or the static disorder.[63,64] Therefore a larger bond distance results in a larger Debye−Waller factor due to stronger thermal vibration, and the presence of static disorder owing to the defect structure or multiple bond distances also induces a large Debye−Waller factor. The present fitted Debye−Waller factors are the order of magnitude of the mean square displacement for the metal−oxygen bond at room temperature, and furthermore Figure 10 shows that there is a linear relationship between the Debye−Waller factors and the Ir−O bond distances. This indicates that the Debye−Waller factors of the Ir−O bonds in the present compounds are surely due to the thermal vibrational effect, and thus the possibility of significant oxygen vacancy or distorted $IrO_6$ octahedron resulting in static disorder, which might cause an abnormally large Debye−Waller factor, can be neglected within the limit of EXAFS spectroscopy. Nevertheless, the coordination numbers obtained from the fit in Table 5 are less than the known coordination number of six in particular for higher oxidation states, although they are within the general error limit[52,65,66] of about 20% ($N = 6 \pm 1.2$). But the fitted coordination numbers, in fact, correspond to the product ($S_0^2N$) of the amplitude reduction factor ($S_0^2$) and the coordination number ($N$), and $S_0^2$ was set equal to unity in the course of the fitting procedure. Therefore if the coordination numbers ($N$) are fixed at 6, $S_0^2$ exhibits values from ~1.1 to ~0.8 having a tendency to decrease with an increase of the oxidation state of the iridium ion as shown in Figure 11. $S_0^2$, which means the square of the overlap between the passive electrons in the initial and final ground states, tends to reduce the EXAFS amplitude and thus often has been phenomenologically introduced to match the experimental and theoretical amplitudes. From this viewpoint, the present results for $S_0^2$ suggest that the oxidation state of the central metal ion should be taken into account in determining the coordination number more exactly. Such results will lead to useful information about the coordination number especially in the case of the transition metal ion which change their oxidation states progressively through chemical reactions such

(63) Sham, T. K. *Acc. Chem. Res.* **1986**, *19*, 99.
(64) Tranquada, J. M.; Ingalls, R. *Phys. Rev. B* **1981**, *28*, 3520.
(65) Via, G. H.; Sinfelt, J. H.; Lytle, F. W. *J. Chem. Phys.* **1979**, *71*, 690.
(66) Lee, P. A.; Citrin, P. H.; Eisenberger, P.; Kincaid, B. M. *Rev. Mod. Phys.* **1981**, *53*, 769.

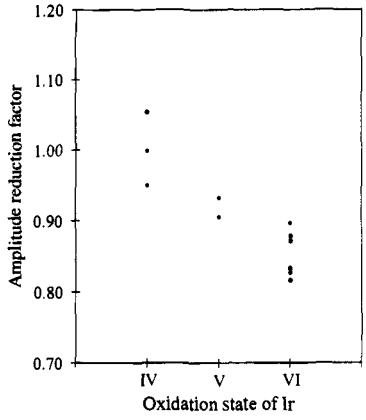


**Figure 11.** Plot of the amplitude reduction factors ($S_0^2$) versus the oxidation state of the iridium. $S_0^2$'s were obtained from the fitted values; $S_0^2N$ with coordination number, $N$, fixed to a known value of 6 under the assumption of no oxygen vacancy expected from the relationship between the Ir−O bond distances and the Debye−Waller factors.

as the redox process. In order to get more general solutions on the relationship between the amplitude reduction factor and the oxidation state of the transition metal ion including the metal−ligand bonding character, systematic research on several transition-metal compounds with various oxidation states is now in progress.

## Conclusion

An accurate $L_{III}$-edge X-ray absorption study has been carried out with respect to the electronic and geometrical structural changes around the iridium ions, which are stabilized in the octahedral sites of the chemically well-characterized perovskite lattices. Previous results on the variation of white line features of the Ir $L_{III}$-edge XANES spectra upon oxidation states of the iridium could be verified more precisely through the present studies. Besides the fact that $e_g$ states directly oriented to ligands are more sensitive to the crystal field than $t_{2g}$ states, the crystal fields on the iridium sites are likely to be varied more significantly with the change of the chemical environment as the oxidation state of the iridium increases. Furthermore, we have, for the first time, examined quantitatively the chemical effects on the Ir−O bond covalency in the various perovskite compounds by means of the Ir $L_{III}$-edge XANES spectroscopy, and these effects have revealed that the qualitative expectation of the degree of covalency through Pauling's ionicity is quite useful and the oxygen vacancy would significantly influence the metal−oxygen bond covalency. The relationship between the difference in the areas for each transition state, $\Delta A$ ($=A_{e_g} - A_{t_{2g}}$), and the oxidation state of the iridium exhibits a good linearity as expected. $SrIrO_3$ shows only a broad peak the same as $IrO_2$, which is different from other iridium compounds and might result from the low vacancy of $t_{2g}$ states when considering the electronic configuration ($t_{2g}^5e_g^0$) of $Ir^{IV}$, in addition to the structurally coupled $IrO_6$ octahedra.

According to EXAFS analyses fot the Ir−O bonding pair in the present perovskite compounds, there is only a single bond distance and no oxygen vacancy within the analytical limit of EXAFS spectroscopy, and these analyses are in good agreement with the splitting to double peaks observed in XANES spectra due to the octahedral crystal field. The average Ir−O bond distances decrease as the iridium oxidation state increases. The ionic radius 0.521 Å of octahedrally coordinated $Ir^{VI}$ could be estimated for the first time from the difference between the experimental $Ir^{VI}$−O bond distance of 1.925 Å and the oxygen ionic radius, 1.404 Å. When the same method was applied for determining the ionic radius of $Ir^{III}$, the estimated value of 0.676 Å was consistent with Shannon's ionic radius (0.68 Å). Furthermore, the tendency of the amplitude reduction factor, $S_0^2$, to decrease with the iridium oxidation state suggests that the oxidation state of the central metal ion should be taken into account when determining the coordination number more precisely. The influences of the oxidation state of the probed metal ions on the EXAFS analysis also have been examined by comparing EXAFS analyses using the experimental model compound and the theoretical standard for $La_2MgIr^{IV}O_6$, $La_2LiIr^{V}O_6$, and $Ba_2CaIr^{VI}O_6$. Consequently, only for the case where unknown and model compounds have the same oxidation state did both analytical methods show similar fitting results as for the unknown, $La_2MgIr^{IV}O_6$, and the model compound, $Ir^{IV}O_2$. These results imply that the oxidation state of the central absorbing atom should be taken into account when the experimental model compounds in EXAFS analysis are used.

**Acknowledgment.** This work was supported by the Korean Ministry of Science and Technology (MOST) in the scope of international cooperation (1994) and in part by the Center for Molecular Catalysis (CMC) and the Korea Science and Engineering Foundation (Grant No. 92-25-00-02). XAS measurements were performed with the approval of the Photon Factory Program Advisory Committee (Proposal No. 92G196). The authors are grateful to Prof. M. Nomura and the Pohang Light Source in Korea (Proposal No. 92-012) for supporting the synchrotron radiation experiments. The Laboratoire de Chimie du Solide du CNRS is acknowledged for supporting the Ph.D. scholarship for D. Y. Jung.

JA950492T